JOURNAL OF COMPUTATIONAL PHYSICS 85, 130–158 (1989)

A Multi-domain Spectral Computation of Three-Dimensional Laminar Horseshoe Vortex Flow Using Incompressible Navier–Stokes Equations

C. S. TAN

Department of Aeronautics and Astronautics, Massachusetts Institute of Technology, Cambridge, Massachusetts 02139

Received March 14, 1988; revised December 29, 1988

The laminar horseshoe vortex flow at a strut–wall intersection is numerically simulated by direct solution of the 3-dimensional incompressible time-dependent Navier–Stokes equations using multi-domain spectral methods. Flow dependence in the direction normal to the wall is represented by direct expansion in Chebyshev polynomials, thus yielding good resolution of the viscous layer at the endwall. However, spatial discretization of flow dependence on the plane parallel to the endwall is done via spectral element method. Such implementation offers the advantages of high-order accuracy, minimal dispersion errors, a degree of geometrical flexibility, and parallelism. The horseshoe vortical flow is characterized by 3-dimensionality, unsteadiness, and a Reynolds number that is large but having viscous effects which are critical to the flow evolution. Time evolution is implemented using a fractional time-stepping technique. Results at low and moderate Reynolds numbers will be presented to demonstrate the application of the method. In these computations, a simple extrapolation outflow boundary condition is used. Difficulty associated with the imposition of the outflow boundary conditions, especially in the endwall flow region near the outflow boundary, is discussed. © 1989 Academic Press, Inc.

1. INTRODUCTION

Although some of the flows encountered in engineering situations can be usefully described by inviscid analyses, there are very often situations in which the viscous effects must be accounted for, even at the most basic level of description. Many of these flows occur in geometries that are inherently 3-dimensional in nature, such as the horseshoe vortex flow at the junction of a strut–wall intersection. The horseshoe vortical flow is characterized by 3-dimensionality, unsteadiness, and a Reynolds number that is "large" but having viscous effects which are critical to the flow evolution. Such flows exist in many situations. For example, horseshoe vortex flow occurs near the junction of an airplane wing with the fuselage [1] and the junction of plate and support in a plate heat exchanger. Another example is present in axial turbomachinery [3] where boundary layers which develop on the annular surfaces of the axial flow passage encounter rows of stationary and rotating blades. The horseshoe vortical flow is of engineering interest because it can lead to flow

0021-9991/89 $3.00
Copyright © 1989 by Academic Press, Inc.
All rights of reproduction in any form reserved.

degradation, high wall shear stresses, high local heat transfer rate and its role as the origin of corner flows. Numerous flow visualization studies [–4] have shown that the horseshoe vortex flow consists of a 3-dimensional boundary layer separation in front of the strut followed by a vortex flow which wraps around the strut. Depending on the Reynolds numbers, there could be more than one horseshoe vortex present, and for a particular flow configuration, there is a critical Reynolds number at which the horseshoe vortical system can become unsteady.

Because of the engineering importance of horseshoe vortex flows and the scarcity of available detailed quantitative flow measurements, many computational methods [5] have been developed for computing and predicting such a flow field. These computational efforts are based purely on the classical finite difference approximations. In the present paper, we describe the computation and prediction of laminar horseshoe vortex flow at moderate Reynolds number by a multi-domain spectral method. Our goal is to arrive at a reliable simulation code that we can use to gain an improved understanding of the vortex flow and the associated corner flows. We

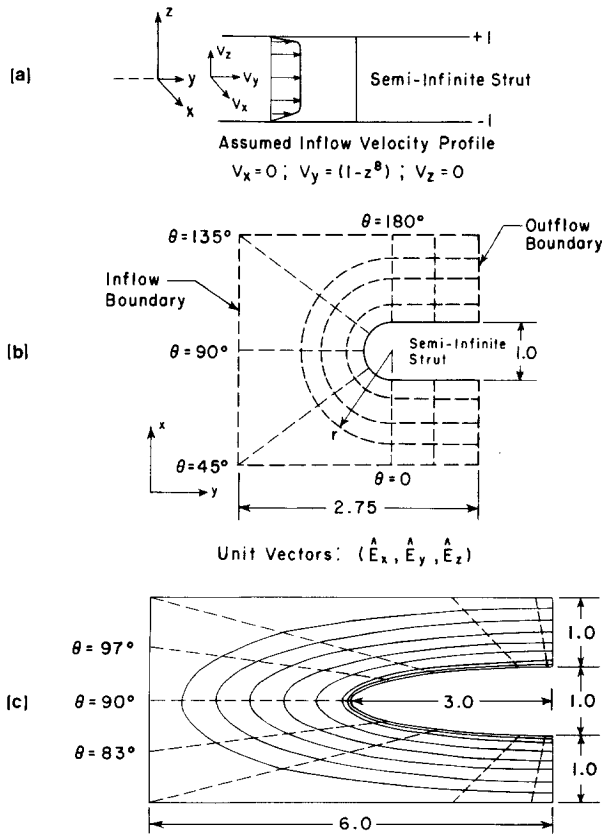

FIG. 1. Coordinate system, nomenclature, and computational domain: (a) Y–Z symmetric plane; (b) semi-infinite strut with circular leading edge; (c) elliptical strut.

also have as our aim to develop and demonstrate the feasibility of the spectral method as a research tool to study and predict fairly complex flow situations of engineering interest. While the heat transfer phenomena is an important facet associated with the horseshoe vortex flow [6] (e.g., in high performance axial turbines), we will not address it in the present paper.

2. Flow Configuration Setup

We shall consider the horseshoe vortex flow to be created by the interaction of a laminar boundary layer on a flat surface and a semi-infinite strut or a finite strut of constant thickness spanned between two parallel flat surfaces. The leading edge of the strut is taken to be circular or elliptical (this is not a restriction). The flow configuration setup is as shown in Fig. 1. The use of the semi-infinite strut assumption essentially eliminates the wake flow region downstream of a finite strut since our primary interest lies in the detailed flow development in the leading edge region. The fact that the strut truncates on the flat surface instead of in the open flow domain facilitates the imposition of the boundary conditions. The flow configuration setup described above is akin to a wind tunnel experiment except that it is done on a computer.

In the following, we will present the development and design of a multi-domain spectral method for the computation of such a fairly complex flow field.

3. The Governing Equations and Time Differencing Scheme

The dynamical equations governing the flow are the incompressible Navier–Stokes equations written in rotational form:

$$\frac{\partial \mathbf{V}}{\partial t} = \mathbf{V} \times \boldsymbol{\omega} - \nabla P_t + \frac{1}{\mathrm{Re}} \nabla^2 \mathbf{V} \tag{1}$$

$$\nabla \cdot \mathbf{V} = 0. \tag{2}$$

Here, $\mathbf{V}$ is the velocity field normalized by the velocity U_m at the center line in the inlet plane, $\boldsymbol{\omega} = \nabla \times \mathbf{V}$ the vorticity field, and $P_t = P + \frac{1}{2}|V|^2$ the total pressure normalized by ρU_m^2; P and ρ are the static pressure and the density of the fluid, respectively. Re is the Reynolds number based on U_m and half the height of the strut. All lengths are normalized by half the strut height so that $\mathrm{Re} = U_m/\nu$ (where ν is the kinematic viscosity). Equation (1) is the momentum equation while Eq. (2) imposes the continuity constraint on the velocity field. In addition to Eqs. (1) and (2), we require the no-slip boundary condition

$$\mathbf{V} = 0 \tag{3}$$

on the strut surface and endwalls. In addition, as Fig. 1 implies, we will choose the computational domain to be a region in the vicinity of the strut that is embedded within a larger overall flow system; consequently we would have to consider "appropriate inflow and outflow boundary conditions" which can adequately model the interface between the computational domain and the remaining flow system. For the flow system considered here, we specify the velocity at the inflow plane so that it consists of a thin shear layer modelling the incoming boundary layer on the flat endwall surfaces and an essentially inviscid core region (see Fig. 1). At the outflow plane, we impose the simple extrapolation outflow boundary condition on $\mathbf{V}$; this is tantamount to saying that the flow does not evolve further in the streamwise direction and hence it constitutes an approximation which one hopes will not contaminate the interior solution.

Given the initial conditions for $\mathbf{V}$ at $t=0$, we choose to advance Eqs. (1) and (2) forward in time using the fractional time-stepping scheme that consists of a nonlinear convective step, a pressure correction step, and a viscous correction step [7]. The nonlinear convective step is implemented through the use of an explicit third-order Adams–Bashforth scheme [15] that yields

$$\hat{\mathbf{V}}^{n+1}-\mathbf{V}^n=\frac{\Delta t}{12}\left[23(\mathbf{V}\times\boldsymbol{\omega})^n-16(\mathbf{V}\times\boldsymbol{\omega})^{n-1}+5(\mathbf{V}\times\boldsymbol{\omega})^{n-2}\right], \tag{3}$$

where the superscript n denotes time level while Δt denotes the chosen time step size. The third-order Adams–Bashforth scheme is chosen for its relatively large stability region near the imaginary axis [8]. It should be noted that, with the exception of the inflow boundary conditions, no other boundary conditions are imposed in this step.

Once the $\hat{\mathbf{V}}^{n+1}$ is determined, we are then left with an unsteady Stokes problem which is split in time as follows. First there is the pressure correction step that consists of

$$\frac{\hat{\mathbf{V}}^{n+1}-\hat{\mathbf{V}}^{n+1}}{\Delta t}=-\nabla P_t, \tag{4a}$$

$$\nabla\cdot\hat{\mathbf{V}}^{n+1}=0, \tag{4b}$$

and

$$\hat{\mathbf{V}}^{n+1}\cdot\hat{e}_n=0 \tag{4c}$$

on the strut surface and endwalls. Technically, the above can also be reformulated as a solution for P_t from

$$\nabla^2 P_t=\nabla\cdot\left(\frac{\hat{\mathbf{V}}^{n+1}}{\Delta t}\right) \tag{5a}$$

subjected to the appropriate inflow/outflow boundary condition (B.C.) and

$$\frac{\partial P_t}{\partial n} = \frac{\hat{\mathbf{V}}^{n+1} \cdot \hat{e}_n}{\Delta t} \tag{5b}$$

on the solid walls. In Eqs. (4c) and (5b), $\hat{e}_n$ denotes the outward normal unit vector on the strut and endwalls. The velocity field $\hat{\mathbf{V}}^{n+1}$ that satisfies the continuity condition is then computed from Eq. (4a).

Following the pressure step is the viscous correction step that imposes the appropriate no-slip boundary conditions on the strut/endwalls and the inflow/outflow boundary conditions on $\mathbf{V}^{n+1}$. This step is discretized in time using the implicit Crank–Nicholson scheme giving

$$\left(\nabla^2 - \frac{2\,\mathrm{Re}}{\Delta t}\right)(\mathbf{V}^{n+1} + \mathbf{V}^n) = -\frac{2\,\mathrm{Re}}{\Delta t}(\hat{\mathbf{V}}^{n+1} + \mathbf{V}^n) \tag{6a}$$

$$\mathbf{V}^{n+1} = \mathbf{V}_m \qquad \text{at the inflow boundary} \tag{6b}$$

$$\mathbf{V}^{n+1} = 0 \qquad \text{at solid wall surface.} \tag{6c}$$

The outflow B.C. imposed is of the simple extrapolation type given here as

$$\frac{\partial \mathbf{V}^{n+1}}{\partial Y} = 0. \tag{6d}$$

Difficulty associated with the imposition of outflow boundary conditions will be discussed further in the section on numerical results.

The above scheme uses the improper inviscid boundary condition on the pressure; it is thus (at least for model problems [9]) of $O(\Delta t)$ accurate in the velocity in the interior of the domain, with larger errors occurring in the pressure and velocity gradients in a boundary layer of thickness $O(\Delta t/\mathrm{Re})^{1/2}$ near the walls [9]. It should be pointed out that Marcus [10] showed that the boundary errors do produce serious inaccuracies in Taylor–Couette flow; he ascribed this to the fact that the dynamics of the Taylor–Couette flow are driven by the motion of the boundary rather than by a mean pressure gradient. As the flow here is driven by the pressure gradient, it can be argued that, at least at moderately high Reynolds number (where $\Delta t/\mathrm{Re}$ is typically small), the above time splitting scheme can achieve comparable accuracy to the higher order methods, with considerably less work and complexity.

We note here that the most expensive numerical operation in stepping the equations forward in time is in inverting the ∇^2 operator for the fairly complex geometry encountered in the horseshoe vortical flow situation. In fact, the inversion must be done four times per time step: once for evaluating the pressure field (Eq. (5a)) and once for each component of the velocity in the viscous fractional step. In the next

section we shall describe a spatial discretization scheme based on the multi-domain spectral method that permits the direct and efficient inversion of the ∇^2 operator for the fairly complex geometry encountered here.

4. Spatial Discretization

4.1. *Coordinate System*

To facilitate the description of spatial discretization used here, we define the following coordinate systems:

(a) The global coordinate system (X, Y, Z). The governing equations, all the discrete differential operators (divergence, curl, gradient, and Laplacian), and the velocity vector

$$\mathbf{V} = V_X \hat{e}_X + V_Y \hat{e}_Y + V_Z \hat{e}_Z \tag{7}$$

will be written in terms of the global coordinate system. In Eq. (7), $(\hat{e}_X, \hat{e}_Y, \hat{e}_Z)$ are the unit vectors and the subscripts (X, Y, Z) denote the vector components in the respective directions. In (X, Y, Z) systems, the endwalls are at $Z = \pm 1$ and the inflow/outflow boundaries are at the constant Y planes. The computational domain is bounded by two constant X planes on either side of the strut (see Fig. 1b). Periodicity of the flow variables is imposed at these constant X planes but *not* at the inflow/outflow planes. Because of this, the flow field is equivalent to that for a cascade of struts of constant pitch in the X direction.

(b) The local coordinate system. This is designed to be a surface-oriented coordinate system. The computational region on the X–Y plane is subdivided into an appropriate number of domains to allow for geometrical and resolution flexibility on the X–Y plane. For subdomains in the vicinity of the circular leading edge of the strut, the appropriate surface-oriented coordinate system to use is the cylindrical coordinate system (r, θ, Z), while away from the leading edge one would preferably choose to use the rectilinear coordinate system (x, y, Z). If an elliptical leading edge is used, one may choose the elliptical coordinate system so as to be surface oriented.

(c) The natural coordinate system (ξ, η, ζ). As in the case of (b), this coordinate system is local to each subdomain but it is so defined that the boundaries of the subdomain are at $\xi = \pm 1$, $\eta = \pm 1$, and $\zeta = \pm 1$.

4.2. *Spatial Discretization in Z*

It has been shown by Orszag [11] that for wall-bounded viscous flows, the no-slip wall boundary condition can be satisfied by using the Chebyshev polynomials as basic expansion functions. Expansions based on these polynomials are highly accurate and have a rate of convergence which depends only on the smoothness of the solution within the domain. Thus, it is natural to represent the flow

dependence in the Z direction by expansion in Chebyshev polynomials. This would also yield high resolution of the boundary layers and viscous layers at the endwalls which are essential facets of the horseshoe vortex flow. However, to incorporate the appropriate boundary conditions (Dirichlet for the velocity in the viscous correction step and Neumann for the pressure correction step) into the expansion, we define an eigenfunction expansion

$$F_l(Z) = \sum_m f_{lm} T_m(Z) \tag{8}$$

to satisfy the Sturm–Liouville problem,

$$\frac{d^2F_l(Z)}{dZ^2} = \lambda_l^2 F_l(Z), \tag{9}$$

where for pressure it is determined to satisfy the homogeneous Neumann boundary condition (since $\partial P/\partial Z = 0$ at $Z = \pm 1$ from Eq. (5b)) while for velocity $\mathbf{V}$, it is determined to satisfy the homogeneous Dirichlet boundary condition (since $\mathbf{V} = 0$ at $Z = \pm 1$). These eigenfunctions can readily be constructed using either the tau method or the collocation method [12]. Reference may be made to [12] for the detailed procedure for constructing such eigenfunctions, including the situation of nonhomogeneous boundary conditions. The Chebyshev polynomials $T_m(Z)$ can be expressed as $T_m(Z) = \cos(m \cos^{-1} Z)$ and we choose the Chebyshev collocation points,

$$Z_k = \cos \frac{\pi k}{L} \tag{10}$$

to yield good resolution of the flow field at the endwalls.

Use of the above procedure esentially decouples the Z-dependence in the Poisson equation for P_t and the Helmholtz equation for $\mathbf{V}$, thus reducing them to a set of 2-dimensional equations (which can simultaneously be solved on a parallel processor, if available). We now proceed to the spatial discretization on the X–Y plane.

4.3. *Spatial Discretization on the X–Y Plane*

It is clear from the layout of the flow configuration on the X–Y plane that it would be extremely difficult to implement the global spectral discretization of the X–Y dependence of the flow variables. Thus we will appeal to the use of a multi-domain spectral method [13–15] for the spatial discretization on the X–Y plane. In particular, we will follow the spectral element discretization technique developed in Refs. [9, 15] for this purpose. Thus the chosen computational domain is subdivided into an appropriate number (say I) of macro-elements as shown in Fig. 1. For a subdomain in the vicinity of the circular leading edge of the strut, the local cylindri-

cal coordinate system is used. In each subdomain, we can then expand the flow variables as

$$\begin{Bmatrix} \mathbf{V} \\ p \end{Bmatrix} = \sum_{j=0}^{N_X} \sum_{k=0}^{N_Y} \sum_{l=0}^{N_Z} \begin{Bmatrix} \mathbf{V}_{jkl} \\ p_{jkl} \end{Bmatrix} h_j^i(\xi^i) h_k^i(\eta^i) F_l(Z), \tag{11}$$

where $h_m(S)$ are high-order local Lagrangian interpolants in terms of Chebyshev polynomials. It can be written as [15]

$$h_m(S) = \frac{2}{M} \sum_{n=0}^{M} \frac{1}{\bar{C}_m \bar{C}_n} T_n(S_m) T_n(S) \tag{12}$$

with

$$\bar{C}_m = \begin{cases} 1 & \text{for } m \neq 0 \text{ or } M \\ 2 & \text{for } m = 0 \text{ or } M \end{cases} \tag{13}$$

and the collocation points S_m given in Eq. (10). It follows from the orthogonality of the discrete Chebyshev series that

$$h_m(S_n) = \delta_{mn}, \tag{14}$$

where δ_{mn} is the Kronecker delta function. In Eq. (11), the superscript i pertains to local subdomain i while the $F_l(Z)$ is the appropriate respective eigenfunction for $\mathbf{V}$ (satisfying the Dirichlet boundary condition) and P_t (satisfying the Neumann boundary condition). Similarly, the mapping from the physical coordinates $(X, Y, Z)^i/(r, \theta, z)^i$ to the local natural coordinates $(\xi, \eta, \zeta)^i$ is given by an isoparametric tensor-product mapping [15],

$$(X, Y)^i = \sum_{j=0}^{J} \sum_{k=0}^{K} (X, Y)_{jk}^i h_j^i(\xi) h_k^i(\eta) \tag{15}$$

as we have taken $Z = \zeta$. We further note that the collocation points in each subdomain are given by

$$(\xi, \eta, Z)_{jkl}^i = \left(\cos \frac{\pi j}{J}, \cos \frac{\pi k}{K}, \cos \frac{\pi l}{L} \right)^i \tag{16}$$

where $\begin{pmatrix} j \\ k \\ l \end{pmatrix}$ runs from $\begin{pmatrix} 0 \\ 0 \\ 0 \end{pmatrix}$ to $\begin{pmatrix} J \\ K \\ L \end{pmatrix}$.

Desirable resolution of flow variables in the $X-Y$ dependence is achieved by an appropriate choice and arrangement of the domain decomposition [15].

5. The Final Discretized Equations

The various semi-discrete differential operators (discrete in the X–Y dependence but continuous in Z) can now be defined in terms of the expansion functions given in Eqs. (8), (9), (11), (12), (15), and (16). They are given in the Appendix.

5.1. *The Nonlinear Convective Step*

Since this step is explicit, it would first involve the evaluation of vorticity $\boldsymbol{\omega}$ in each subdomain according to

$$\begin{aligned}\boldsymbol{\omega}_{jkl} = &\left\{\frac{1}{J_{jk}}\sum_{p=0}^{N_X}\sum_{q=0}^{N_Y}\sum_{r=0}^{N_Z}\tilde{\nabla}_{Yjkpq}V_{Xpqr}T_r(Z_l)\right.\\ &\left.-\sum_{p=0}^{N_X}\sum_{q=0}^{N_Y}\sum_{r=0}^{N_Z}V^{(1)}_{Ypqr}T_r(Z_l)\right\}\hat{e}_X\\ &+\left\{\sum_{p=0}^{N_X}\sum_{q=0}^{N_Y}\sum_{r=0}^{N_Z}V^{(1)}_{Xpqr}T_r(Z_l)\right.\\ &\left.-\frac{1}{J_{jk}}\sum_{p=0}^{N_X}\sum_{q=0}^{N_Y}\sum_{r=0}^{N_Z}\tilde{\nabla}_{Xjkpq}V_{Zpqr}T_r(Z_l)\right\}\hat{e}_Y\\ &+\left\{\frac{1}{J_{jk}}\sum_{p=0}^{N_X}\sum_{q=0}^{N_Y}\sum_{r=0}^{N_Z}\tilde{\nabla}_{Xjkpq}V_{Ypqr}T_r(Z_l)\right.\\ &\left.-\frac{1}{J_{jk}}\sum_{p=0}^{N_X}\sum_{q=0}^{N_Y}\sum_{r=0}^{N_Z}\tilde{\nabla}_{Yjkpq}V_{Xpqr}T_r(Z_l)\right\}\hat{e}_Z,\end{aligned}\tag{17}$$

where $V^{(1)}_{pqr}$ is evaluated [16] according to, for each p and q,

$$\mathbf{V}^{(1)}_{pqr}=\frac{2}{C_r}\sum_{l=r+1}^{N_Z}l\mathbf{V}_{pql}.\tag{18}$$

In Eq. (17), J_{jk} is the Jacobian of the geometrical mapping, while C_r in Eq. (18) is given as

$$\begin{aligned}C_r &= 2 \quad \text{for} \quad r=0\\ &= 1 \quad \text{for} \quad r>0.\end{aligned}$$

The subscript jkl refers to the collocation points of Eq. (16). The value of the vorticity along the inter-element boundaries, say between element a and element b, is taken as the weighted average [15],

$$\omega_{\text{inter-element boundary}}=\tfrac{1}{2}\omega_a\,|\,{}_{\text{boundary}}^{\text{at inter-element}}+\tfrac{1}{2}\omega_b\,|\,{}_{\text{boundary}}^{\text{at inter-element}}\tag{19}$$

The nonlinear term $(\mathbf{V}\times\boldsymbol{\omega})$ is evaluated by the collocation technique since the convolution sums required by the Galerkin formulation are costly to evaluate [16]. Thus, this step amounts to the update of $\hat{V}_{jkl}^{n+1}$ from

$$\hat{\mathbf{V}}_{jkl}^{n+1}=\mathbf{V}_{jkl}^{n}+\frac{\Delta t}{12}\left(23(\mathbf{V}\times\boldsymbol{\omega})_{jkl}^{n}-16(\mathbf{V}\times\boldsymbol{\omega})_{jkl}^{n-1}+5(\mathbf{V}\times\boldsymbol{\omega})_{jkl}^{n-2}\right). \tag{20}$$

Only the inflow boundary condition is imposed at this step.

5.2. *The Pressure Correction Step*

In the solution for the total pressure head P_t, we will choose not to discretize Eq. (5a) directly [15], but rather we first formulate the weighted residual form of the continuity condition (Eq. (4b)) over the (X, Y)-dependence (or (ξ, η)-dependence) based on $h_j(\xi)h_k(\eta)$ but keeping the Z-dependence. This leads to a semi-discretized continuity condition given as

$$\begin{aligned}\sum^{i}\sum_{j}\sum_{k}\sum_{l}\sum_{m}-[\tilde{\tilde{\nabla}}^{i}_{Xjkpq}\tilde{\tilde{\nabla}}^{i}_{Yjkpq}][\tilde{\tilde{B}}^{i}_{jklm}]\begin{bmatrix}\hat{V}^{n+1}_{Xlm}(Z)\\ \hat{V}^{n+1}_{Ylm}(Z)\end{bmatrix}+\sum_{j}\sum_{k}\overset{+}{B}{}^{i}_{pqjk}\left(\frac{\partial\hat{V}^{n+1}_{Z}}{\partial Z}\right)_{jk}\\ =\sum_{k}\sum_{m}\sum_{s}Y_{N_X s}D_{sk}\tilde{B}_{kmq}\hat{V}^{n+1}_{XN_Ym}(Z)\delta_{pN_X}+\sum_{j}\sum_{l}\sum_{r}X_{rN_Y}D_{rj}\tilde{B}_{jlp}\hat{V}^{n+1}_{YlN_Y}(Z)\delta_{qN_Y}\\ -\sum_{k}\sum_{m}\sum_{s}Y_{1s}D_{sk}\tilde{B}_{kmq}\hat{V}^{n+1}_{X1m}(Z)\delta_{p1}-\sum_{j}\sum_{l}\sum_{r}X_{r1}D_{rj}\tilde{B}_{jlp}\hat{V}^{n+1}_{Yl1}(Z)\delta_{q1}.\end{aligned} \tag{21}$$

The notation $\sum^{i}$ means taking account of all the contributions from all the subdomains (i.e., application of direct stiffness procedure as in the finite element technique) [17]. The first two terms on the RHS of Eq. (21) refer to the specified incoming flow while the last two terms refer to the outgoing flow. The semi-weighted residual form of Eq. (4a) is

$$\sum_{j}\sum_{k}\tilde{\tilde{B}}_{pqjk}[\hat{V}^{n+1}_{Xjk}-\hat{V}^{n+1}_{Xjk}]=-\sum_{j}\sum_{k}\sum_{r}\sum_{s}\bar{B}_{pqjk}\tilde{\tilde{\nabla}}_{Xjkrs}P_{t_{rs}}\Delta t \tag{22a}$$

$$\sum_{j}\sum_{k}\tilde{\tilde{B}}_{pqjk}[\hat{V}^{n+1}_{Yjk}-\hat{V}^{n+1}_{Yjk}]=-\sum_{j}\sum_{k}\sum_{r}\sum_{s}\bar{B}_{pqjk}\tilde{\tilde{\nabla}}_{Yjkrs}P_{t_{rs}}\Delta t \tag{22b}$$

$$\sum_{j}\sum_{k}\overset{+}{B}{}_{lmjk}[\hat{V}^{n+1}_{Zjk}-\hat{V}^{n+1}_{Zjk}]=-\sum_{j}\sum_{k}\overset{+}{B}{}_{lmjk}\left(\frac{\partial P_t}{\partial Z}\right)_{jk}\Delta t. \tag{22c}$$

From Eqs. (21) and (22) one can obtain a consistent equation for P_t as

$$\sum{}^{i}\sum_{r}\sum_{s} A_{lmrs} P_{t_{rs}}(Z)\,\Delta t + \sum_{r}\sum_{s} \overset{+}{B}_{lmrs}\left(\frac{\partial^2 P_t}{\partial Z^2}\right)_{rs}\Delta t$$

$$= \sum{}^{i}\Bigg\{ -\sum_{j}\sum_{k}\sum_{p}\sum_{q} \tilde{\tilde{\nabla}}_{Xpqlm}\tilde{\tilde{B}}_{pqjk}\hat{V}^{n+1}_{Xjk} - \tilde{\tilde{\nabla}}_{Ypqlm}\tilde{\tilde{B}}_{pqjk}\hat{V}^{n+1}_{Yjk} \qquad \text{(I)}$$

$$+ \sum_{j}\sum_{k} \overset{+}{B}_{lmjk}\left(\frac{\partial \hat{V}^{n+1}_{Z}}{\partial Z}\right)_{jk}\Bigg\}$$

$$- \sum_{k}\sum_{m}\sum_{s} Y_{N_X s} D_{sk}\tilde{B}_{kmq}\hat{V}^{n+1}_{XN_X m}(Z)\delta_{pN_X} \qquad \text{(II)}$$

$$- \sum_{j}\sum_{l}\sum_{r} X_{rN_Y} D_{rj}\tilde{B}_{jlp}\hat{V}^{n+1}_{YlN_Y}(Z)\delta_{qN_Y} \qquad \text{(III)}$$

$$+ \sum_{k}\sum_{m}\sum_{s} Y_{1s} D_{sk}\tilde{B}_{kmq}\hat{V}^{n+1}_{X1m}(Z)\delta_{p1} \qquad \text{(IV)}$$

$$+ \sum_{j}\sum_{l}\sum_{r} X_{r1} D_{rj}\tilde{B}_{jlp}\hat{V}^{n+1}_{Yl1}(Z)\delta_{q1} = \tau_{lm}(Z), \qquad \text{(V)} \qquad (23)$$

where

$$A_{lmrs} = -\sum_{j}\sum_{k}\sum_{p}\sum_{q} \tilde{\tilde{\nabla}}_{pqlm}\cdot \bar{B}_{pqjk}\tilde{\tilde{\nabla}}_{jkrs}. \qquad (24)$$

We will choose to determine the pressure P_t consistently from Eq. (23). For the present problem, we note that the implementation of the inflow/outflow boundary condition simply requires the specification of the last four terms on the RHS of Eq. (21); in particular, because of the assumed inflow velocity, the second (II) and fourth (IV) terms on the RHS of Eq. (23) can be taken to be zero for the 3-dimensional horseshoe vortical flow situation considered here and the remaining two terms (i.e., the third and fifth) are simply the incoming flow and the outgoing flow. Therefore, their presence is to modify the sum of the first two terms on the RHS at collocation points along the inflow and outflow boundaries in consistence with the continuity requirement. Quantities like $\tilde{B}_{jlp}$, $\bar{B}_{pqjk}$, and $\overset{+}{B}_{jklm}$ that appear in the above equations are given in the Appendix.

Next, we proceed to use Eq,. (9) to separate out the Z-dependence so that Eq. (23) is reduced to a set of 2-dimensional equations given as

$$\sum{}^{i}\sum_{j}\sum_{k} A_{pqjk}(P_t)_{jkl} + \lambda_l^2 \sum_{j}\sum_{k} \overset{+}{B}_{pqjk}(P_t)_{jkl} = \tau_{pql}, \qquad (25)$$

where the subscript l in the above equation refers to the projection of $(P_t)_{jk}$ in the physical space Z to the eigenvector space of $F_l(Z)$ via Eq. (8).

5.3. *The Viscous Correction Step*

We first employ Eq. (9) to separate out the Z-dependence so that Eq. (6) is reduced to a set of 2-dimensional equations with (X, Y)-dependence, given as

$$\left(\frac{\partial^2}{\partial X^2}+\frac{\partial^2}{\partial Y^2}-\frac{2\,\mathrm{Re}}{\Delta t}+\lambda_l^2\right)(\mathbf{V}^{n+1})_l=\left(-\frac{2\,\mathrm{Re}}{\Delta t}\hat{\mathbf{V}}^{n+1}-\nabla^2\mathbf{V}^{2n}\right)_l=(\boldsymbol{\sigma})_l, \tag{26}$$

where the subscript l in Eq. (26) refers to the projection of $\mathbf{V}_{jk}$ in physical space Z to the eigenvector space of $F_l(Z)$. Note that each of the sets of equations described by Eqs. (25) and (26) can be solved independently of one another, thus resulting in parallelism of implementation.

We can now appeal to the equivalence of the differential Eq. (26) with the extremization of the functional [17]

$$I(V^{n+1})=\int_X\int_Y\left[-\frac{1}{2}\left(\frac{\partial V_l^{n+1}}{\partial X}\right)^2-\frac{1}{2}\left(\frac{\partial V_l^{n+1}}{\partial Y}\right)^2-\frac{\lambda_l^2}{2}(V_l^{n+1})^2-(V_l)^{n+1}\sigma_l\right]dX\,dY \tag{27}$$

with restriction to admissible variations associated with the essential boundary conditions in Eqs. (6b) and (6c). Equation (27) refers to a component of Eq. (26). We now use Eq. (11) and the geometric transformation Eq. (15) in the functional Eq. (27), perform the resulting integration and seek the stationarity of the functional with respect to variation in V_{jkl}^{n+1} [9, 15, 17] to arrive at

$$\sum_j^{i}\sum_k\sum\left\{A_{pqjk}+\lambda_l^2\overset{+}{B}_{pqjk}-\frac{2\,\mathrm{Re}}{\Delta t}\overset{+}{B}_{pqjk}\right\}\mathbf{V}_{jkl}^{n+1}=\sum_j\sum_k\overset{+}{B}_{pqjk}\boldsymbol{\sigma}_{jk}. \tag{28}$$

The above discretization technique allows the natural satisfaction of the imposed outflow boundary condition (Eq. (6d)), while the inflow boundary condition and the no-slip boundary condition on the strut surface are implemented via static condensation [15, 17].

However, if a different type of outflow boundary other than the simple extrapolation kind (e.g., the advective type of outflow boundary condition) is used, the functional I should be appropriately modified to reflect its use.

5. Numerical and Computational Implementation

The sequential steps which are performed for a complete computational cycle are presented below.

(1) *Preprocessing Stage*

The following quantities are computed once for all in the preprocessing phase of the computation:

(a) The eigenvalues λ_l, the eigenvectors, and their inverses associated with the diagonalization of the Chebyshev-tau approximation to $\partial^2/\partial Z^2$, one set for the pressure step with homogeneous Neumann boundary condition and another for the viscous step with homogeneous Dirichlet boundary condition at $Z = \pm 1$.

(b) The matrices $Y_{N_X s} D_{sk} \tilde{B}_{kmq} \delta_{pN_X}$, $X_{rN_Y} D_{rj} \tilde{B}_{jlp} \delta_{qN_Y}$, $Y_{1s} D_{sk} \tilde{B}_{kmq} \delta_{p1}$, $X_{r1} D_{rj} \tilde{B}_{jlp} \delta_{q1}$, $\overset{+}{B}_{jklm}$, A_{lmrs}, $\bar{\nabla}_{jkpq}$, $\bar{B}_{pqjk} \bar{\nabla}_{jkrs}$, and $\bar{\nabla}_{pqlm} \tilde{\bar{B}}_{pqjk}$.

(c) The matrices corresponding to the solution of Eqs. (25) and (28) by the static condensation method [17] (there is one set corresponding to each value of λ_l). These matrices are symmetric and their inverses are computed through symmetric factorization.

(2) *Computational Cycle*

(a) Given the initial data (i.e., the initial conditions), a simple forward Euler time-stepping method with a considerably smaller time step size is used to obtain the second time level. The second-order Adams–Bashforth scheme is then used to obtain the third time level.

(b) With the three time levels of the velocity field from the previous calculation or from (a), the RHS of Eq. (20) can be evaluated to advance the velocity field to $\hat{\mathbf{V}}_{jkl}^{n+1}$.

(c) The RHS of Eq. (23) is appropriately evaluated and the result is matrix-multiplied by the appropriate inverse of the eigenvectors. The solution of $(P_t)_{jkl}$ is then obtained from Eq. (25) by the static condensation technique [15, 17]. The multiplication of $(P_t)_{jkl}$ by the appropriate eigenvectors will yield $P_t(X_j, Y_k, Z; t)$; a divergence-free velocity field $\hat{\hat{\mathbf{V}}}^{n+1}$ is then computed from Eq. (22).

(d) Using a similar procedure for the implementation of (c), the velocity field $\mathbf{V}^{n+1}$ that satisfies the non-slip wall boundary condition is obtained via Eqs. (6) and (28).

(e) The velocity field and the pressure field corresponding to the next time cycle is obtained by repeating steps (b) to (d).

The computer code based on the above numerical algorithm has been designed to take advantage of the availability of the SSD-device on the Cray XMP at NASA Lewis. To illustrate this point, consider the case with a resolution of 33 Chebyshev terms for the Z-dependence and 100 subdomains with a 7 by 7 Chebyshev series interpolant in each of the subdomains that make up the computational domain on the X–Y plane. The use of the factorization (diagonalization) technique based on the tau-approximation for the Z-dependence reduces the 3-dimensionality of the pressure step and viscous correction step to a set of 31 two-dimensional problems. This fact together with the explicitness of the nonlinear convective step permits the implementation of each fractional step by solution of a 2-dimensional problem one at a time in the core memory, while the other 30 two-dimensional ones reside on the SSD-device. A brute force approach to a 3-dimensional Navier–Stokes solution

with such a resolution would easily exceed the core memory capacity of the Cray XMP. An alternative to the direct solution technique presented here is the use of the iterative technique [18], such as the preconditioned conjugate gradient method, which may demand more CPU time.

7. *Numerical Results*

In this section we present numerical results for 3-dimensional horseshoe vortex flow from the application of the computer code designed in accordance with the above numerical scheme. Results for struts of two different geometries are presented here: (1) a semi-infinite strut of thickness 1.0 with a semi-circular leading edge (Fig. 1b), and (2) an elliptical strut with a ratio of major to minor axis of 6.0 (Fig. 1c). In all cases, the velocity profile at the inflow plane is such that $V_X = 0$, $V_Y = (1 - Z^8)$, $V_Z = 0$. The shear in velocity at the endwalls afforded by V_Y can be thought of as representing the boundary layer in the approaching flow.

Steady state results for strut (1) are obtained for Reynolds numbers from 50 to 500. For these examples, the pitch is of 4.0 units and the inflow boundary is at a distance of 2.0 units (i.e., about two diameters) upstream of the strut (i.e., at $Y = 0.0$). The spatial resolution used for these calculations is 33 Chebyshev polynomial terms in the spanwise direction (i.e., Z-direction) and 32 subdomains on the X–Y plane, where in each subdomain the flow variables are spatially resolved using 7 by 7 Chebyshev collocation points. The time step used for these calculations is 0.0025. Typical residual history for the three velocity components is shown in Fig. 2; for the case of a Reynolds number of 300, it takes about 2000 time steps for the residual to decay to about 10^{-7}. Figures 3a to 3f show the vector plot of the velocity projection on a r–Z plane for $\theta = 90°$ to $\theta = 180°$ (Fig. 1b), and on an X–Z

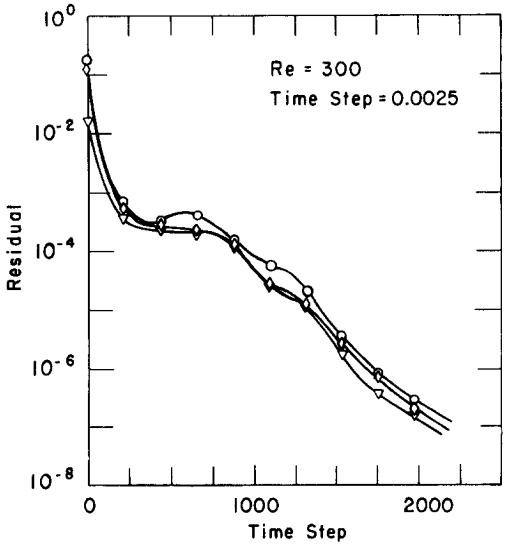

FIG. 2. Convergence history to steady state.

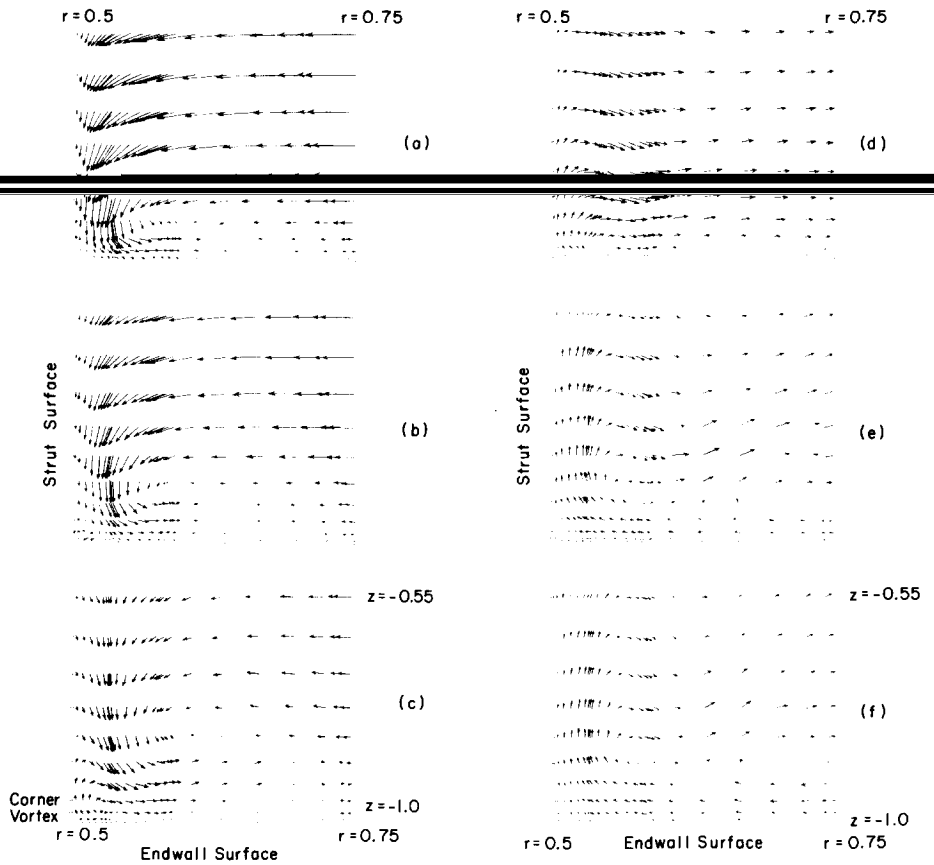

FIG. 3. Velocity projection on various r–z planes showing the evolution of vortical system for Re = 300. Each r–z plane extends from $r = 0.5$ (strut surface) to $r = 0.75$ and from $z = -1.0$ (endwall surface) to $z = -0.55$: (a) at $\theta = 90°$ plane; (b) at $\theta = 135°$ plane; (c) at $\theta = 157.5°$ plane; (d) at 180° plane (i.e., $Y = 2.0$); (e) at $Y = 2.50$ plane; (f) at $Y = 2.75$ plane (outflow plane).

plane for $Y = 2.00$ to 2.75, which is the outflow boundary. These planes only extend from $Z = -1.0$ (endwall) to $Z = -0.55$ and from $r = 0.5$ to 0.75 (or $X = 0.5$ to 0.75 in Figs. 3e and f) so that the local details of the flow evolution from the leading edge plane to the outflow plane can better be elucidated. On the leading edge plane (i.e., $\theta = 90°$ plane in Fig. 3a), the flow is downward in regions close to the strut surface; the flow direction is upstream away from the strut in the immediate vicinity of the endwall up to a radial location of about 0.61. A stagnant flow region appears around a radial location of 0.64. The flow direction is all downstream towards the strut upstream of radial location $r = 0.67$. The results in Figs. 3b and c are essentialy similar to that in Fig. 3a except that there appears to be an incipient formation of a corner vortex at the junction between the strut and the endwall. The flow features seen in Figs. 3a to c are due to the presence of a laminar horseshoe vortex formed

around the base of the strut accompanied by the separation of the approaching boundary layer flow. The formation of a corner vortex and its subsequent growth acts to displace the horseshoe vortex away from the strut and endwall into the core flow (Fig. 3c). In particular, as seen in Fig. 3c, the corner vortex induces an upward flow along the strut surface (between $Z = -1.0$ and -0.83), while the displaced core of the horseshoe vortex induces a downward flow along the strut surface.

As one proceeds further downstream to the outflow boundary (i.e., Figs. 3d to f), the corner vortex grows in size with consequent displacement of the horseshoe vortex core (which appears quite diffused at about $Y = 2.50$) into the main flow. A closer look at Figs. 3e and f would lead one to deduce that the stagnant flow region referred to in Figs. 3a to d (as will be deduced from Fig. 7, this stagnant flow region must be in the immediate neighborhood of the line of separation) might have resulted in an additional endwall vortex; its sense of rotation is the same as the corner vortex but opposite to that of the horseshoe vortex. The results in Figs. 3e and f show that the flow in the endwall region is toward the strut from $X = 0.75$ to 0.66, at which point it turns upward before proceeding in a direction away from the strut; this can essentially be attributed to the presence of an endwall vortical region as indicated in Fig. 3f. The existence of a corner vortex, a horseshoe vortex, and an endwall vortex is more clearly illustrated in Fig. 4. The computational result shown there is for the same flow configuration at $\theta = 157.5°$ plane downstream from the leading edge, but at a lower Reynolds number of 150 (rather than 300). The endwall vortex appears earlier in this case. One could conceivably argue that the displacement and the movement of these vortices could be explained in terms of their induced flow field as well as that of their images.

Such a vortical system has actually been observed in flow through a low speed experimental cascade rig for a turbine blade row [19, 20] representative of that

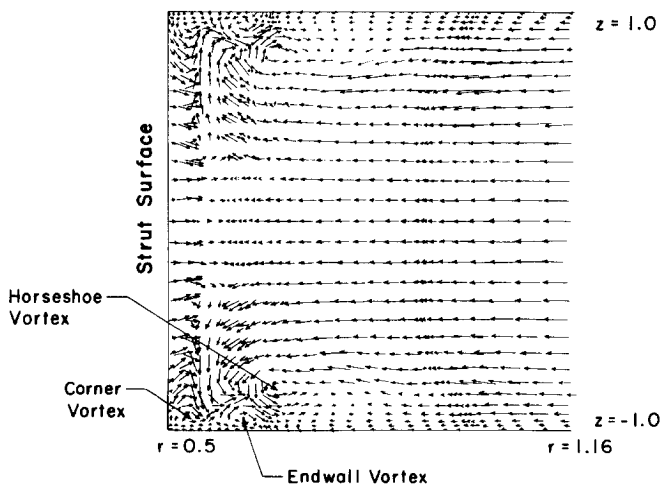

FIG. 4. The vortical system (looking upstream from a downstream station) for computational results at $\mathrm{Re} = 150$ and at $\theta = 157.5°$.

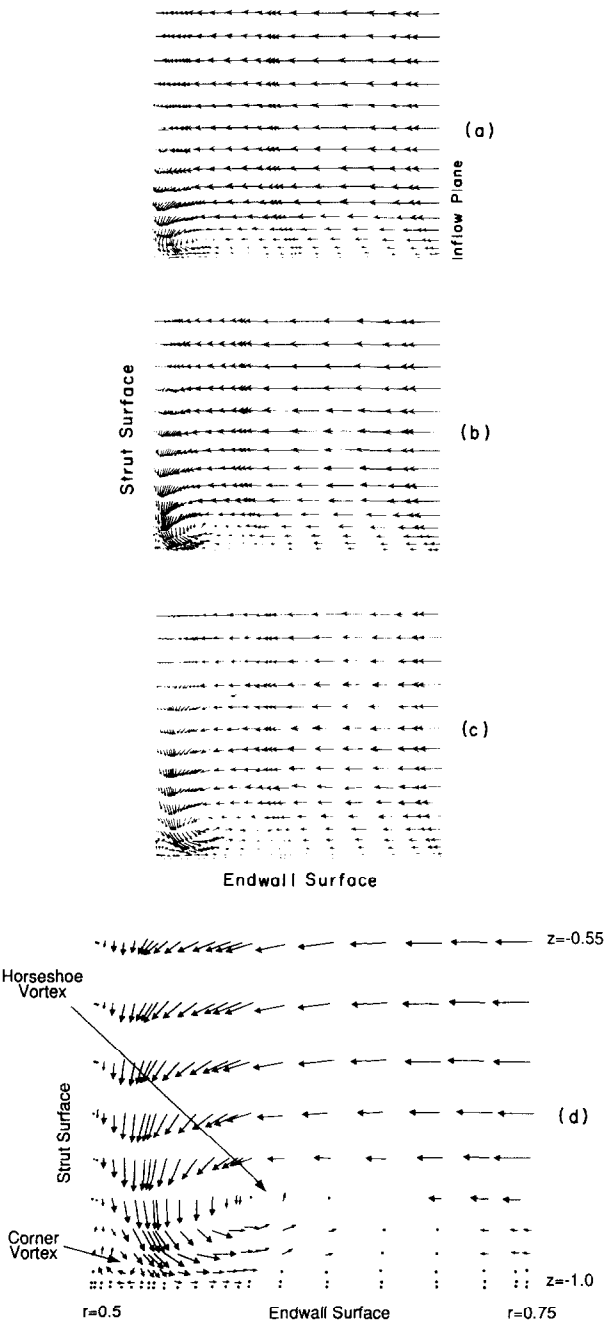

FIG. 5. Velocity projection on various r–z planes indicating the evolution of vortical system for Re = 500. Each r–z plane extends from strut surface to outer boundary of computational domain and from endwall suface ($z = -1.0$) to mid-span ($z = 0.0$): (a) at $\theta = 90°$ plane; (b) at $\theta = 146.35°$ plane; (c) at $\theta = 157.5°$ plane. (d) Enlarged view of Fig. 5b showing the vortical flow field in detail.

used in modern aero-engines. Such qualitative agreement is rather fortuituous as the numerical results are of a rather low Reynolds number (300) flow, while the experimental data pertains to a high Reynolds number flow in a situation that mimics a real technological device.

The results for Reynolds number 500 are presented in Fig. 5, which shows the vector plot of velocity projection on the r–Z plane from $\theta = 90°$ to 157.5°, and in Fig. 6 which shows the vector plot of the velocity projection on the X–Y plane at $Z = -0.99$ (i.e., the grid-plane adjacent to the endwall surface) and at $Z = -0.98$ (i.e., the next grid-plane up). The vortical feature of the flow in Fig. 5 is essentially the same as that shown in Fig. 3. Figure 5d shows an enlarged view of Fig. 5b to bring out the vortical structure. In Fig. 6, a stagnation point of flow (Figs. 6a and b) (i.e., point of attachment) followed by a saddle point type of flow separation (Figs. 6c and d) upstream of the leading edge are evident [21]. The numerical results in Figs. 3 to 6 would lead one to deduce a limiting streamline pattern as shown in Fig. 7a on the endwall surface and in Fig. 7b on the surface of the circular leading edge of the strut [21].

In the course of obtaining these results, it was found that adequate resolution of the viscous layers at the endwalls and strut surface, as well as in the artificial boundary layer at the outflow boundary (due to the imposition of a simple extrapolation outflow boundary condition), is very critical to maintaining the stability of the numerical solution for a long time. Insufficient resolution in these

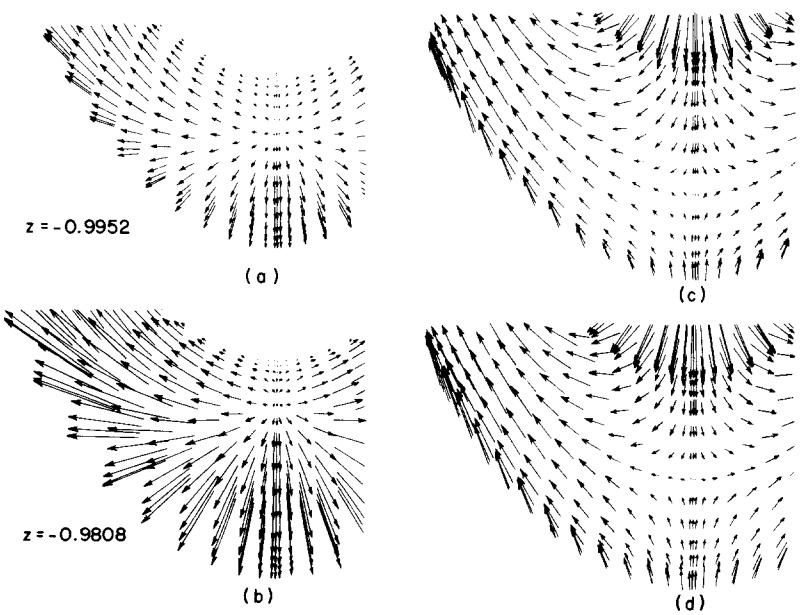

FIG. 6. Velocity projection on two planes adjacent to the endwall showing the topological features of the flow field: (a, b) indicate presence of a stagnation point flow, while (c, d) indicate presence of a saddle point of separation.

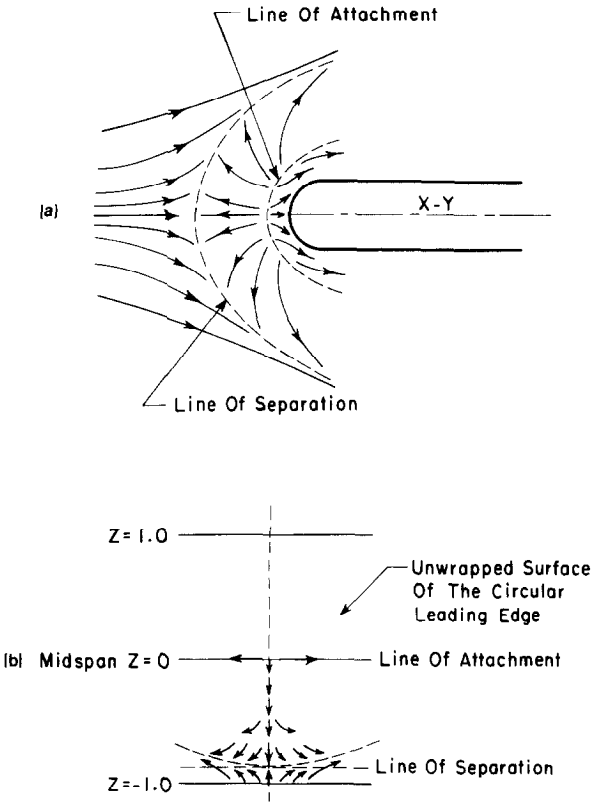

FIG. 7. Limiting streamline feature as deduced from the numerical results: (a) on the endwall surface; (b) on the surface of the circular leading edge of the strut.

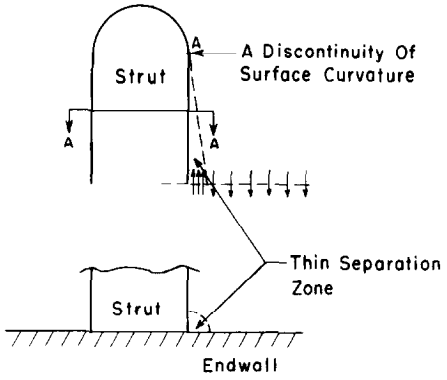

FIG. 8. Sketch illustrating the presence of a thin separation zone as deduced from the numerical results.

layers results in oscillating behavior of the solution there which will then destroy the solution ultimately. Attempts were made to obtain a solution for a Reynolds number of 750 to 900 in this geometry, but with 60 to 80 subdomains for the X–Y dependence. However, in this range of Reynolds numbers, the computed results show that the flow at the endwall region separates at point A (Fig. 8), where there is a discontinuity in surface curvature. There is thus a thin separation zone at the corner between the strut and the endwall that stretches from point A to the outflow boundary as indicated in Fig. 8. Because of this, backflow occurs at the outflow boundary in this thin separation zone, and stable numerical solutions cannot be maintained for a very long time.

zone, semi-elliptical struts are adopted (i.e., geometry of type 2, see Fig. 1c). There

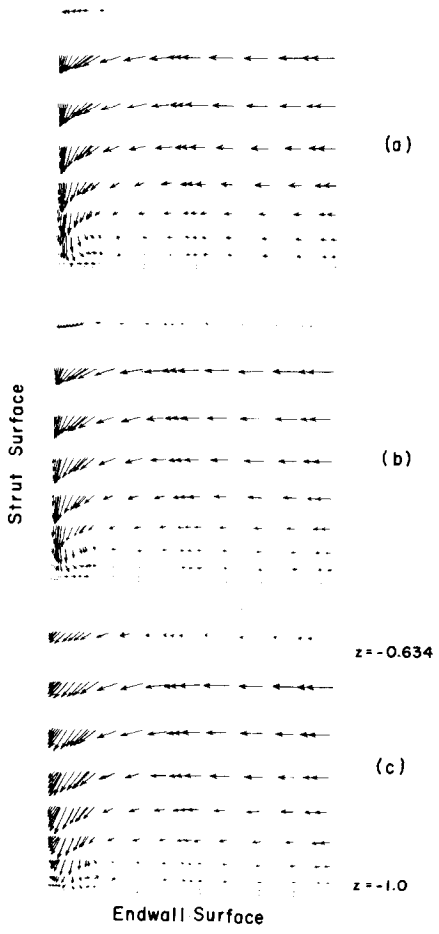

FIG. 9. Velocity projection on r–z planes indicating the presence of a leading edge horseshoe vortex for an elliptical strut at $\mathrm{Re} = 650$. Each r–z plane extends from the strut surface and from $z = -1.0$ (endwall surface) to $z = -0.634$: (a) at $\theta = 90°$ plane; (b) at $\theta = 90.5°$ plane; (c) at $\theta = 91.75°$ plane.

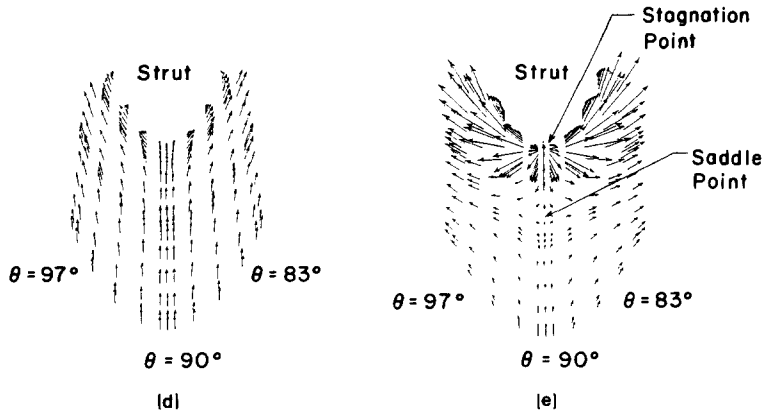

FIG. 9—*Continued.* Velocity projection on $z =$ constant planes: (d) midspan plane at $z = 0.0$; (e) endwall plane at $z = -0.99$.

is no discontinuity in surface curvature for this geometry. Solutions for Reynolds numbers of 400 and 650 were obtained. We show the results for a Reynolds number of 650. Figures 9a, b, c show the vector plots of the velocity on the r–Z plane at $\theta = 90°$ (leading edge plane), 90.5°, and 91.75°, while Figs. 9d, *e* show the velocity vector plot on two X–Y planes: one at midspan and the other close to the endwall. These results indicate the presence of a horseshoe vortex with the accompanying endwall boundary layer separation giving rise to a saddle point of separation. The next figure shows the streamwise vorticity distribution on a r–Z plane at various θ-locations. The streamwise vorticity ω_S is computed according to

$$\omega_S = \omega_X\left(\frac{V_X}{V_S}\right) + \omega_Y\left(\frac{V_Y}{V_S}\right) + \omega_Z\left(\frac{V_Z}{V_S}\right),$$

where

$$V_S = \sqrt{V_X^2 + V_Y^2 + V_Z^2}.$$

As in the previous examples, downstream of the leading edge we observe the formation of a corner vortex and an endwall vortex of the opposite sense to that of the horseshoe vortex.

The static pressure coefficient C_p (defined as $C_p = (P - P_{-\infty})/\rho U_m^2$, where $P_{-\infty}$ is the value far upstream) is shown in Figs. 11; Figs. 11a and b show respectively the C_p distribution on the endwall surface and on an X–Y plane near the mid-span, while Fig. 11c shows the C_p distribution on the surface of the elliptical strut. As one would expect, the presence of the strut has given rise to a region of adverse pressure gradient upstream of the strut which in turn leads to flow separation at the endwall region; this is also consistent with the presence of a horseshoe vortex near the leading edge of the strut. In Fig. 11c, the presence of a spanwise pressure gradient toward the endwall is consistent with the downward endwall flow caused by the

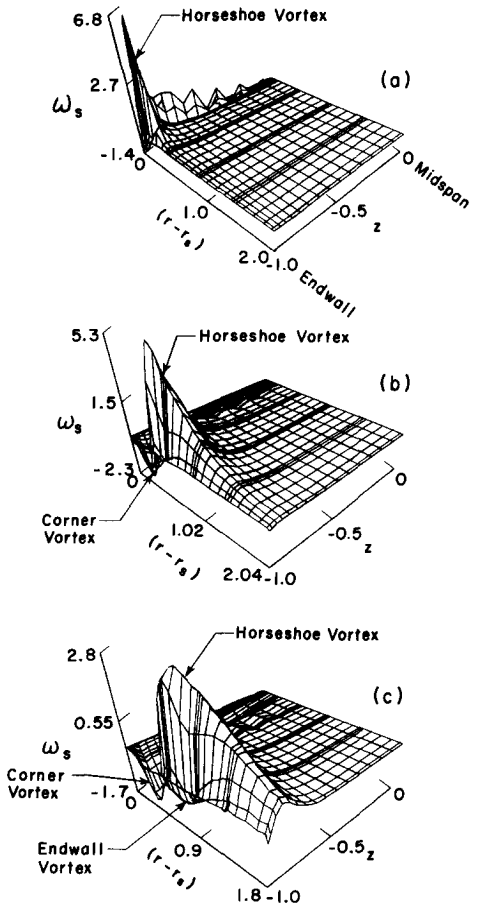

FIG. 10. Development of streamwise vortices in the case of an elliptical strut with Re = 650: (a) at $\theta = 90°$ plane; (b) at $\theta = 97°$ plane; (c) at $\theta = 102°$ plane. $r - r_s = 0$ is the strut surface.

presence of the horseshoe vortex flow. The corresponding total pressure coefficient distribution at various locations in the flow domain are shown in Figs. 12a to c. These results indicate that, in the endwall flow region near the leading edge of the strut, the total pressure actually increases near the strut leading edge; in certain regions of the endwall flow, the increase in total pressure is not monotonous for the increase but is followed by a decrease in total pressure towards the strut surface. However, near the mid-span region, the fluid particle essentially maintains its total pressure level until in a region very close to the strut. The above observations in the numerical results are not surprising at all for the horseshoe vortex does not consist always of the same fluid but draws in fresh supplies constantly from the upstream core flow which is at a higher total pressure.

To demonstrate the influence of the boundary conditions imposed at the outflow

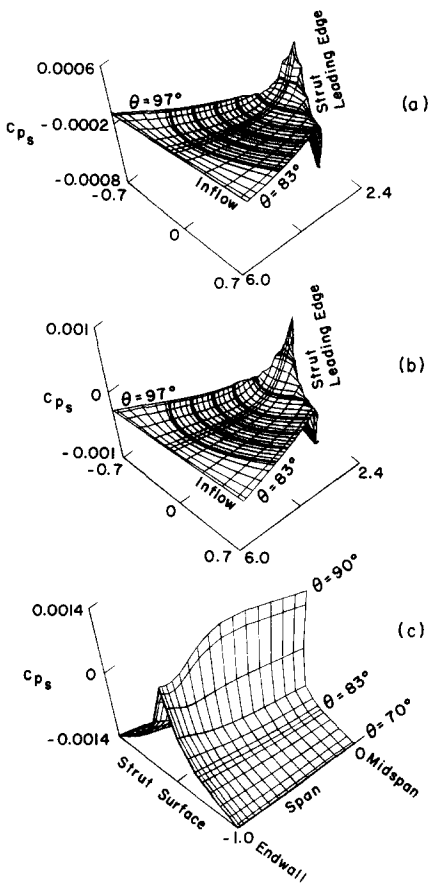

FIG. 11. Static pressure distribution: (a) on endwall plane between inflow and strut leading edge; (b) at midspan plane between inflow and strut leading edge; (c) on surface of elliptical strut. Re = 650.

boundary, we will now show the numerical results in the flow domains adjacent to the outflow boundary. The static pressure coefficient distribution at various constant Z planes is shown in Fig. 13, and the corresponding results for the vector plot of the velocity are shown in Fig. 14. Because of the imposition of a simple extrapolation outflow boundary condition, an artificial boundary layer forms at the outflow boundary [22]. In particular, one observed the presence of an adverse pressure gradient region (marked X in the figure) away from the strut. However, the fluid in the endwall region may have difficulty negotiating this adverse pressure gradient; in the present example, this results in a very slight reverse flow followed by velocity streaming towards the strut and then out of the computational domain. It appears that this adverse pressure gradient poses no problem at all to the numerical solution or the flow away from the endwall region as the results of Fig. 14 attest.

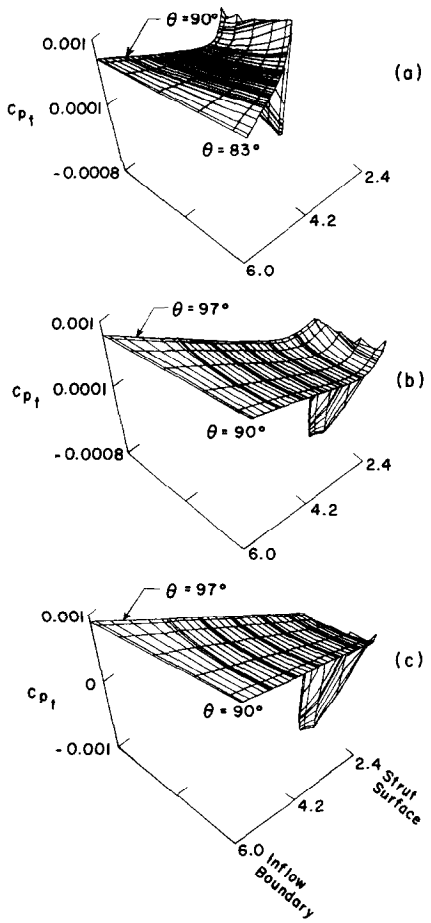

FIG. 12. Total pressure distribution in the endwall region at $z = -0.83$ in (a), at $z = -0.77$ in (b), and at midspan $z = 0.0$ in (c) for the case of elliptical strut with $\mathrm{Re} = 650$.

When the Reynolds number of the flow is increased to 1000 with the same spatial resolution as that for the Reynolds number of 650, the velocity at the outflow region (corresponding to where the adverse pressure gradient is) evolves, after about 100 times steps (each time step is 0.0025), to a state shown in Fig. 15; the velocity oscillates and alternates in direction even in a region far away from the endwall; the results in Fig. 15 pertain to that at midspan, and the result in the endwall region is worse. Examination of the numerical solution shows that the solution in the leading region looks fine. Further time advancement leads to eventual breakdown of the numerical solution. However, when the spatial resolution is increased to 100 subdomains with resolution refinement in the outward direction from the strut (i.e., spatial resolution is refined in a direction normal to the flow at the outflow boundary), a stable solution for a Reynolds number of 1000 can be

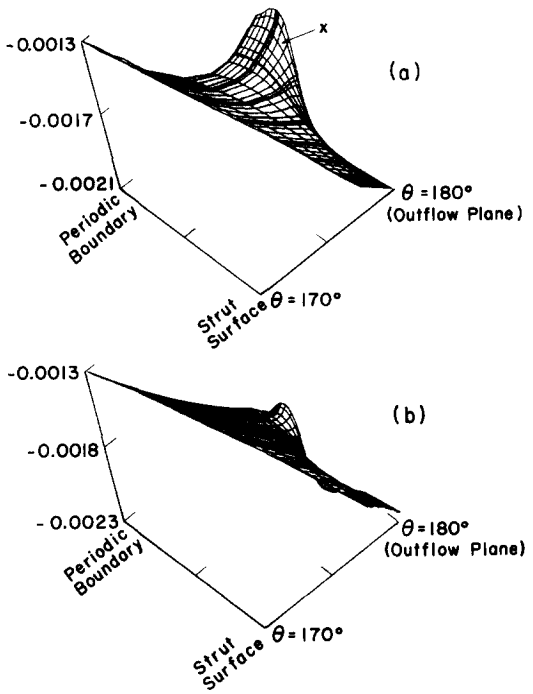

FIG. 13. Static pressure distribution on the subdomains preceding the outflow boundary indicating the presene of an adverse pressure gradient: (a) at $z = -1.0$ (endwall); (b) at $z = 0.0$ (midspan).

maintained to 1000 time steps. At this stage, the flow features are similar to the case of $\mathrm{Re} = 650$.

The current computer code takes about 0.3×10^{-3} s per time step per degree of freedom to implement on a Cray-XMP. It should also be mentioned that the code has not been fully vectorized nor optimized in terms of computer usage. Typically, with a resolution of 161,700° of freedom and with the use of a Cray solid-state storage device, it requires 1.5 MW of core memory for execution.

8. Concluding Remarks

The multi-domain spectral method is applied to the computation of a fairly complex 3-dimensional horseshoe vortex flow (laminar) at the strut–endwall junction representative of many engineering situations of interest. The numerical solutions at moderate Reynolds numbers show flow features associated with horseshoe vortical flow that have been observed in experiments. Flow dependence in the direction of the span of the strut is represented by a Chebyshev series while, on a plane normal to the strut, discretization by a spectral element scheme is adopted. Steady state

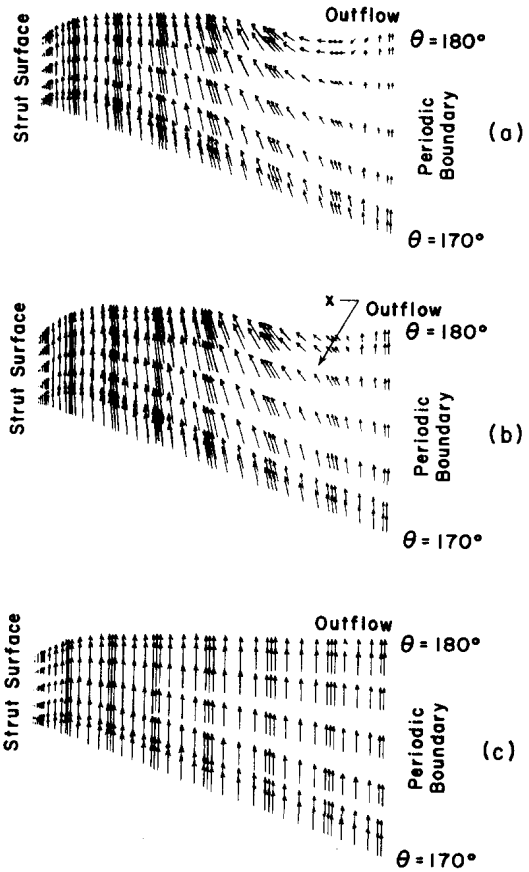

FIG. 14. Velocity projection on $z =$ constant planes in the endwall region as well as at midspan preceding outflow plane for elliptical strut with $\mathrm{Re} = 650$: (a) at $z = -0.99$; (b) at $z = -0.98$; (c) at $z = 0.0$.

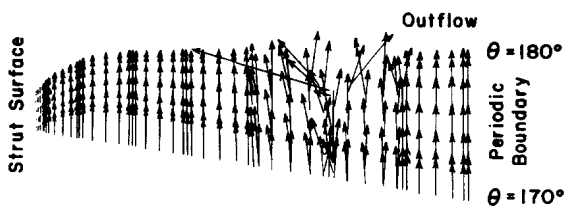

FIG. 15. Velocity on midspan plane ($z = 0.0$) preceding outflow boundary indicating solution breakdown due to insufficient spatial resolution (elliptical strut with $\mathrm{Re} = 1000$).

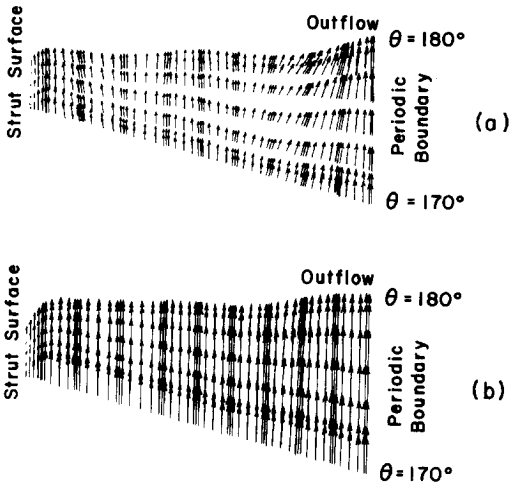

FIG. 16. Velocity projection on an endwall plane and midspan plane preceding outflow boundary indicating a stable solution with increased spatial resolution (elliptical strut with Re = 1000): (a) at $z = 0.99$; (b) $z = 0.0$.

solutions for Reynolds numbers of 50 to 650 are obtained. In the course of obtaining the above solutions, it was found that adequate resolution of the viscous layers at the endwalls and the strut surface, as well as the downstream artificial boundary layers (especially in the endwall region), due to the imposition of a simple extrapolation outflow boundary condition, are very critical to the stability of the numerical solution; for the *present problem*, not only should the downstream artificial boundary layer be well resolved spatially in the streamwise direction, but it must also be well resolved spatially in a direction normal to the streamwise flow; this is especially so in the endwall region. For the cases computed here, the presence of the downstream boundary layer arising from the imposed outflow boundary condition does not appear to contaminate the flow phenomena of interest in the leading edge region.

It was also found that discontinuity in the surface curvature could lead to a separation zone with reverse flow at the corner between the strut and endwall that stretches out to the outflow boundary. In this case, further refinement of the spatial resolution at the outflow boundary does not appear to help in stabilizing the solution. A different kind of outflow boundary condition (e.g., advective type) other than the simple extrapolation type used here may help. As the Reynolds number of the flow increases, a numerical solution for the present problem can only be attained with difficulty. The present examples suggest that the principal difficulty is at the outflow boundary. It may be possible to alleviate this difficulty by locally enhancing the fluid viscosity in the vicinity of the outflow boundary [22], in this case, a different solution algorithm from that used here would have to be adopted.

APPENDIX

The gradient operator ∇ operating on a scalar f yields

$$\nabla f = \frac{1}{J}\tilde{\nabla}_{2D} f + \frac{\partial f}{\partial Z}\hat{e}_Z, \tag{A1}$$

where J is the Jacobian of the geometrical mapping between (X, Y, Z) and (ξ, η, Z), and $\tilde{\nabla}_{2D}$ is given as

$$\tilde{\nabla}_{2D} f = \left(Y_\eta \frac{\partial f}{\partial \xi} - Y_\xi \frac{\partial f}{\partial \eta}\right)\hat{e}_X + \left(X_\xi \frac{\partial f}{\partial \eta} - X_\eta \frac{\partial f}{\partial \xi}\right)\hat{e}_Y. \tag{A2}$$

The operator $\tilde{\nabla}_{2D}$ is constructed following Ref. [15]. Thus the semi-discrete $(\nabla f)_{jk}$ can be written as

$$(\nabla f)_{jk} = \frac{1}{J_{jk}} \sum_{p=0}^{N_X} \sum_{q=0}^{N_Y} \tilde{\nabla}_{2Djkpq} f_{pq}(Z) + \sum_{p=0}^{N_X} \sum_{q=0}^{N_Y} \frac{\partial f_{pq}}{\partial Z} h_p(\xi_j) h_q(\eta_k)\hat{e}_Z, \tag{A3}$$

where $\tilde{\nabla}_{jkpq}$ is given by [15]

$$\begin{aligned}\tilde{\nabla}_{jkpq} &= D_{pj}(Y_\eta)_{pk}\delta_{qk} + D_{qk}(-Y_\xi)_{jq}\delta_{pj}\hat{e}_X \\ &\quad + D_{pj}(-X_\eta)_{pk}\delta_{qk} + D_{qk}(X_\xi)_{jq}\delta_{pj}\hat{e}_Y \\ &= \tilde{\nabla}_{Xjkpq}\hat{e}_X + \tilde{\nabla}_{Yjkpq}\hat{e}_Y.\end{aligned} \tag{A4}$$

The discrete differential operator D_{jp} on the Chebyshev collocation grid within each subdomain is simply given by [15]

$$D_{jp} = \frac{d}{dS} h_j(S_p), \tag{A5}$$

where δ_{pq} is the Kronecker delta function; the subscripts X, Y, and Z have been used to denote the component in the X, Y, and Z direction, respectively; (X_{jk}, Y_{jk}) denotes collocation points corresponding to $\xi_j = \cos \pi j/N_X$ and $\eta_k = \cos \pi k/N_Y$; quantities like B_{jlp}, B_{pqjk}, and B_{jklm} are given as [15]

$$\tilde{B}_{jlp} = \int_{-1}^{+1} h_j(\zeta) h_l(\zeta) h_p(\zeta)\, d\zeta$$

$$\tilde{\tilde{B}}_{pqjk} = \operatorname{sign}(J)\left(\sum_r \tilde{B}_{rpj}\right)\left(\sum_s \tilde{B}_{sqk}\right)$$

$$\overset{\pm}{B}_{jklm} = \sum_p \sum_q |J_{pq}| \overset{\pm}{} \tilde{B}_{jlp}\tilde{B}_{kmq}.$$

ACKNOWLEDGMENTS

The author is grateful to Dr. J. Adamczyk of NASA Lewis for many helpful suggestions as well as for making the author's various visits to NASA Lewis an enjoyable experience. He also thanks Professor A. Patera of MIT for various discussions on the numerics, and Mr. M. Celestina, Mr. R. Mulac, and Dr. W. To of Sverdrup for their invaluable help on many aspects of the usage of computer systems at NASA Lewis. The work was supported through NASA Lewis Grant NAG3-660, Dr. J. Adamczyk Program Manager.

REFERENCES

1. B. THWAITES, *Incompressible Aerodynamics* (Oxford Univ. Press, London, 1960).
2. C. J. BAKER, Ph.D. thesis, University of Cambridge, England, 1978; *J. Fluid Mech.* **95**, 347 (1979).
3. T. J. BARBER, *J. Aircraft* **15** (1978).
4. A. S. W. THOMAS, *Phys. Fluids* **30**, No. 2 (1987).
5. W. R. BRILEY AND H. MCDONALD, "Computation of Three-Dimensional Horseshoe Vortex Flow Using the Navier–Stokes Equations," 7th Int. Conf. on Numerical Methods in Fluid Dynamics, 1980.
6. R. J. GOLDSTEIN AND J. KARNI, *Trans. ASME J. Heat Transfer* **106** (1984).
7. S. A. ORSZAG AND L. KELLS, *J. Fluid Mech.* **96** (1980).
8. W. C. GEAR, *Numerical Initial Value Problems in Ordinary Differential Equations* (Prentice–Hall, Englewood Cliffs, NJ, 1971).
9. A. T. PATERA, *J. Comput. Phys.* **54**, 468 (1984).
10. P. MARCUS, *J. Fluid Mech.* **146** (1984).
11. S. ORSZAG, *J. Fluid Mech.* **49** (1971).
12. C. S. TAN, *J. Comput. Phys.* **59**, No. 1 (1985).
13. B. METIVET AND Y. MORCHOISNE, in *Proceedings, 4th GAMM Conference on Numerical Methods in Fluid Mechanics*, edited by H. Viviand (Vieweg, Brunswick, 1982).
14. M. MACARAEG AND C. L. STREETT, *Appl. Numer. Math.* **2**, 95 (1986).
15. K. Z. KORCZAK AND A. T. PATERA, *J. Comput. Phys.* **62**, 361 (1986).
16. P. GOTTLIEB AND S. ORSZAG, *Numerical Analysis of Spectral Methods: Theory and Applicaion* (SIAM, Philodelphia, 1977).
17. G. STRANGE AND G. FIX, *An Analysis of the Finite Element Method* (Prentice–Hall, Englewood Cliffs, NJ, 1973).
18. A. PATERA, Massachusetts Institute of Technology, Cambridge, MA, private communication, 1987.
19. E. RENAUD, Massachusetts Institute of Technology, Cambridge, MA, private communication, 1987.
20. O. SHARMA, Pratt & Whitney Aircraft Co., Hartford, CT, private communication, 1987.
21. O. ROSENHEAD (Ed.), *Laminar Boundary Layer* (Oxford Univ. Press, London, 1963).
22. D. B. HAIDVOGEL, *J. Comput. Phys.* **33** (1979).